**FEATURED ARTICLES**

# Impedance of Porous Electrodes

View the article online for updates and enhancements.

## You may also like

# Impedance of Porous Electrodes

*by Yiming Zhang, Kei Ono, Jianbo Zhang*

Electrochemical processes, including electric double-layer charging and discharging, electrosorption of reaction intermediates and electrolytes, and charge-transfer reactions, occur at the electrode-electrolyte interface (EEI). Maximizing the rates of these electrochemical processes requires increasing the electrode's surface area while maintaining efficient mass transport. Porous electrodes meet these competing requirements by introducing interconnected pore networks into the electrodes.

Porous electrodes are essential in a variety of electrochemical devices, including electrochemical energy devices, sensors, and electrochemical synthesis. Porous electrodes are also, unfortunately, involved in various corrosion processes. The catalyst layers (CL) in polymer electrolyte fuel cells (PEFCs) and the electrodes in lithium-ion batteries (LIBs) are good examples because of their widespread commercialization, richness in both theoretical treatment and engineering exploration, and distinct features in structure and functionality.

A fuel cell is a device that converts the chemical energy of gaseous fuels and oxidants into electrical energy through electrochemical processes. Fig. 1a shows a schematic of the structure of a typical PEFC. The close-ups on the right depict the mass transfer of the reacting species at the three-phase interface (TPI) near platinum (Pt) particles for oxygen reduction reaction (ORR) at the cathode and hydrogen oxidation reaction (HOR) at the anode. As the oxygen and hydrogen diffuse across the pores in the CL to the reaction sites, this type of porous electrode is referred to as a gas diffusion electrode (GDE). The ORR is notoriously sluggish and constitutes the rate-limiting step of the electrochemical processes in PEFCs. Since the best electrocatalyst for ORR in acid media is based on the precious metal Pt, the priority in CL design is to maximize the effective use of the Pt.

The effective use of Pt can be enhanced through three key strategies: (1) finely dispersing nanosized Pt particles on carbon supports, (2) constructing a proton-conducting ionomer network in the CL, and (3) optimizing reactant/product transport in the porous electrode. The efficiency of mass transport depends sensitively on the operating conditions such as the current density and the levels of humidification. Liquid water saturation in pores tends to increase under high current densities or degraded pore surface hydrophobicity. Such flooding of the GDE, which severely impedes $O_2$ diffusion and incurs significant concentration overpotential, is one scenario that has attracted extensive R&D efforts. Conversely, drying of the GDE near the inlet under low or no humidification, or operating at high temperature (T>90 °C), reduces the proton conductivity of the membrane and the ionomer in CL, resulting in significant ohmic as well as activation losses. The complex interplay among multiple processes in the CL, gas diffusion layer (GDL), and flow channel determines how robustly the fuel cell operates and how effectively Pt can be utilized at high current densities.

A LIB, operating via the reversible intercalation and deintercalation of Li ions to and from the active materials, is an electrochemical device for both energy storage and energy conversion. Fig. 1b shows a cross-sectional SEM image of the positive and negative electrodes in a typical LIB. The close-ups on the right show the pathways of lithium ions and electrons relative to the positive and negative active materials during discharge.

The design priority for LIB electrodes is to balance the competing requirements of energy density and power density. Increasing the energy density requires a greater volume fraction of active materials in the electrodes, yet overly compacted electrodes cannot accommodate high charging/discharging rates and therefore compromise power capability. As the volume fraction of solid contents in the electrode is typically greater than that of the pores, the LIB electrodes are often termed composite electrodes. As electrolyte permeates the electrode pores, this type of porous electrode is also referred to as flooded electrodes.
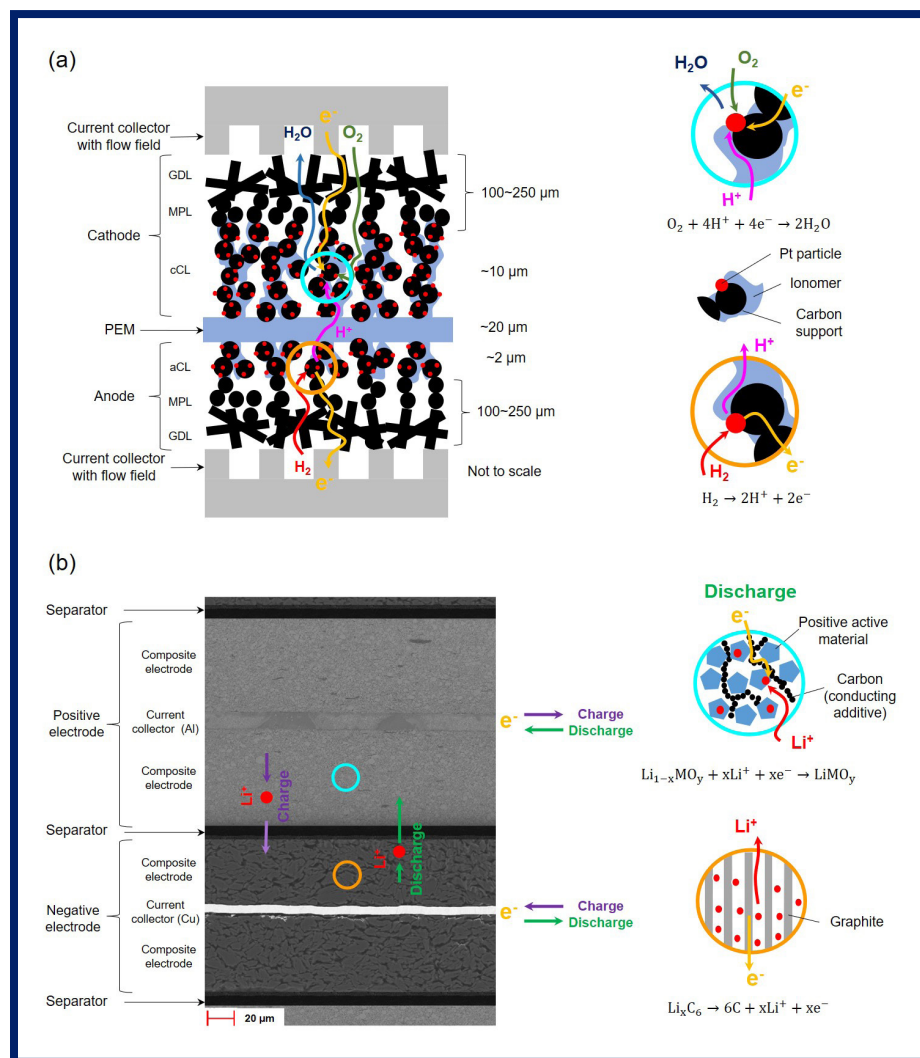


**Fig. 1.** *(a) Schematic (left) and close-ups (right) of a typical PEFC. (b) Cross-sectional SEM image of the positive and negative electrodes (left) and close-ups (right) of a typical LIB.*

Table I compares the major characteristics of the porous electrodes in PEFCs and LIBs. PEFCs employ GDEs with thin and highly porous CL to reduce gas diffusion losses. In contrast, LIBs employ thick, flooded, and densely compacted composite electrodes to ensure sufficient storage capacity for Li ions while maintaining low ionic and electronic resistances.

To optimize electrode design in response to ever-increasing demand, both electrochemical methods (including time and frequency domains) and physicochemical characterization methods (including element, morphology, and structure analysis, etc.) are needed to characterize the porous electrodes. Under ideal conditions, the direct current (DC) method in the time domain and the alternating current (AC) method in the frequency domain contain the same information, and are mathematically interconvertible. However, under realistic conditions, factors such as noise, equipment resolution, and the information content at different frequencies may favor one method over the other. Generally speaking, time-domain methods are well-developed for studying steady or transient state problems. In contrast, EIS is powerful in resolving multiple processes occurring at well-separated characteristic frequencies, which is just the case for porous electrodes.

## Features and Signatures of EIS of Porous Electrodes

Fig. 2 compares the Nyquist-format impedance spectra of electrodes across three pairs of charts: blocking electrodes (Fig. 2a and 2b), cathode in fuel cells at a certain current density (Fig. 2c and 2d), and intercalation electrodes in LIBs at a certain open-circuit voltage (OCV) (Fig. 2e and f). Each pair contrasts the responses of flat (left) versus porous (right) electrodes with red curves showing theoretical predictions and blue schematics representing typical experimental data. To facilitate the intra-/inter-plot comparison, units and numerical values of the impedance are not included. The direction of increasing frequency is indicated by an arrow along the spectrum from the model prediction.

The EIS of porous electrodes under blocking conditions is commonly employed to characterize their ohmic and structural properties. A blocking electrode operates in an inert atmosphere without electroactive species within the tested potential range, thus preventing faradaic current. Consequently, the system simplifies to include only double-layer charging and discharging processes.

## Difference Between Blocking and Non-Blocking Electrodes

The primary difference in impedance spectra between blocking (Fig. 2a and 2b) and non-blocking electrodes (Fig. 2c–2f) is the presence or absence of semicircles in the intermediate frequency range. These semicircles arise from the charge-transfer reactions of electroactive species or the adsorption and desorption of the intermediates, impurities, or electrolytes. Each semicircle contributes a new time constant to the spectra. More time constants make it more challenging for EIS to resolve the underlying processes.

In the low frequency range, the blocking electrode demonstrates capacitive behavior corresponding to the electric double layer (Fig. 2a and 2b). In contrast, the fuel cell spectra converge toward the real axis, following the behavior of planar Warburg impedance under finite-length diffusion boundary conditions (Fig. 2c and 2d). The LIB spectra in the low frequency range also show a capacitive behavior (Fig. 2e and 2f). However, this behavior is attributed to the charging and discharging of the active materials, rather than the electric double layer.

## Difference Between Flat and Porous Electrodes

The primary difference in the spectra between flat and porous electrodes is the slope of the high-frequency intercept with the real axis. The model predicts slopes of 90° for the flat electrodes and

| **Table I. Comparison of the Porous Electrodes in PEFCs and LIBs** | | |
|---|---|---|
| | **PEFCs** | **LIBs** |
| Type of devices | Energy conversion | Energy conversion and storage |
| Type of thermodynamic system | Open | Closed |
| Type of porous electrode | Gas-diffusion, partially wetted electrode | Composite, flooded electrode |
| Limiting step/process | ORR | Li dendrite formation |
| Current density range | 0.2~0.6 A/cm² (standard operation) 0.8~2 A/cm² (peak power operation) | 0.3~1.5 mA/cm² (energy type) 2~10 mA/cm² (power type) |
| Typical values of electrode parameters | Thickness: ~10 µm Porosity: 30~70% Tortuosity: 2~5 Specific area: 60~1000 m²/g$_c$ ECSA: ~50 m²/g$_{Pt}$ Roughness factor: ~100 (@0.2 mg$_{Pt}$/cm²) (@0.2 mg$_{Pt}$/cm²) | Thickness: ~100 µm Porosity: 30%~40% Tortuosity: 3~6 Specific area: 20 m²/g$_{LFP}$, 60 m²/g$_c$ -- -- |
| Ionic conductivity (bulk) and conduction mechanism | ~0.1 S/cm Migration ($t_{H^+}$ =1) | ~0.01 S/cm Diffusion/migration ($t_{Li^+}$=0.36) |
| Electronic conductivity | Low for non-PGM catalyst | Low in positive electrode |

45° for the porous electrodes. An electrode behaves more like a flat electrode than a porous one when the pore depth is sufficiently small, or the porosity is sufficiently large, or the ionic impedance is sufficiently lower than the interfacial impedance:

$$\frac{a_V l_p^2}{\kappa_{e,eff} Z_{loc}} \ll 1 \qquad (1)$$

where $a_V$ is the volumetric electrochemical surface area, $l_p$ is the thickness of the porous electrode, $\kappa_{e,eff}$ is the effective ionic conductivity, and $Z_{loc}$ is the local impedance at the electrode/electrolyte interface.

Under these conditions, the penetration depth of the AC signal is significantly greater than the pore depth (the electrode thickness). Consequently, the impedance of the porous electrode $Z_{pe}$ is equivalent to the interfacial impedance $Z_{loc}$ diminished by the roughness factor:

$$Z_{pe} = \frac{Z_{loc}}{a_V l_p} \qquad (2)$$

Such a porous electrode is essentially a rough electrode, serving as a transition between flat and porous electrodes. Its spectra do not display a 45° line segment at the high-frequency region. Therefore, a line segment with a 45° slope at the high-frequency region, whether under blocking or non-blocking conditions, can be considered a signature of a porous electrode.

Line segments with slopes of 1/2 or 1/4 of 45° have been measured and analyzed through modeling. Itagaki explained the halving of the slopes for activated carbon capacitors from the effects of a double or triple fractal structure within the carbon particles.[16] Huang predicted the 22.5° slope observed for an electrode composed of secondary particles in LIBs with a three-scale impedance model,[2] and asserted that the slope of the line segment halves with each increase in the scale of the microstructure. To the best of the authors' knowledge, line segments with slopes approximating 22.5° have not been reported in PEFCs. This absence suggests that the agglomerate model may not accurately represent the true structure of CLs in PEFCs. The format of
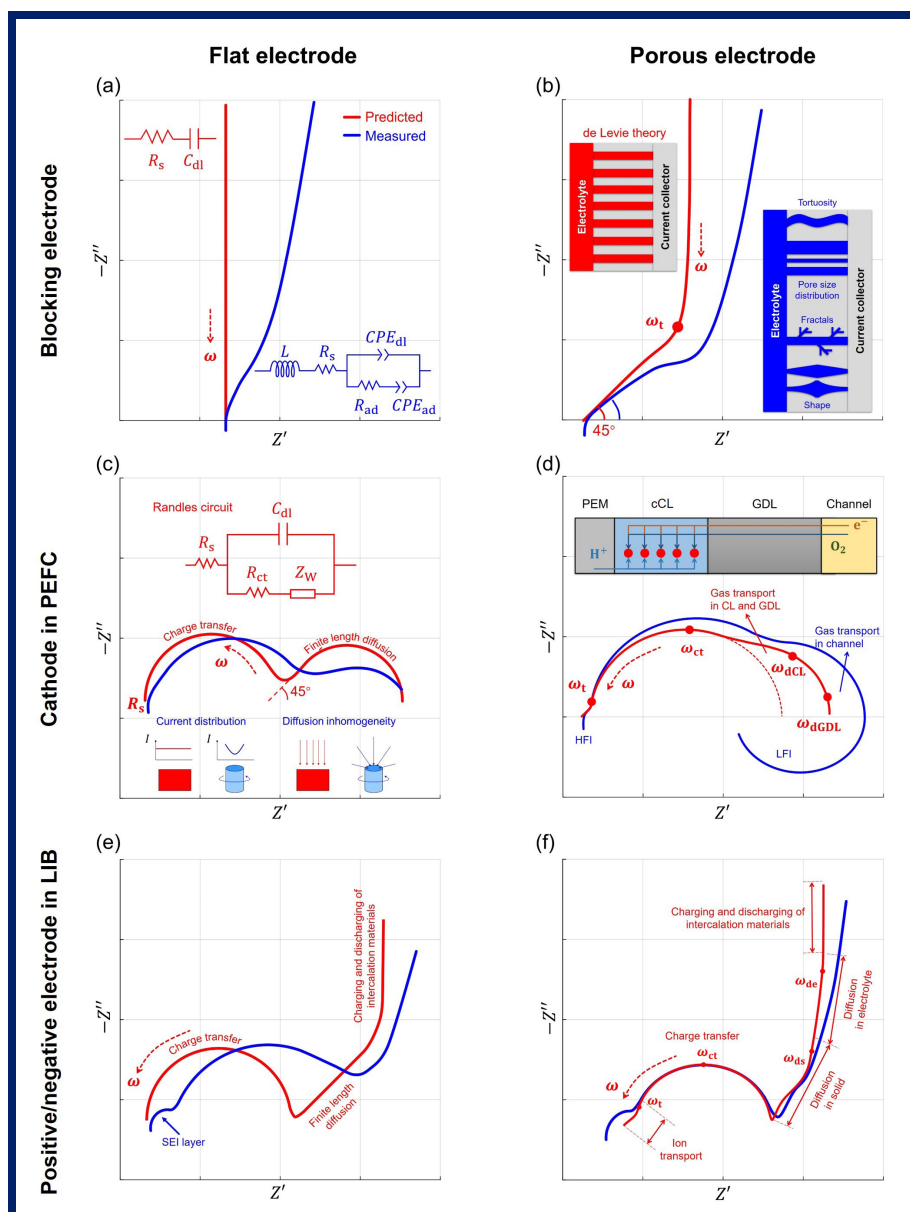
**Fig. 2.** *Nyquist-format impedance spectra for (a) flat blocking electrode, (b) porous blocking electrode ($\omega_t$ is the characteristic frequency of ion conduction), (c) flat cathode in fuel cell, (d) porous cathode in PEFC ($\omega_c$, $\omega_{dCL}$ and $\omega_{dGDL}$ are the characteristic frequencies of charge transfer, gas diffusion in CL and gas diffusion in GDL, respectively), (e) flat intercalation electrode, (f) porous positive/negative electrode in LIB ($\omega_{ds}$ and $\omega_{de}$ are the characteristic frequencies of diffusion in solid and diffusion in electrolyte, respectively). The formulas for the characteristic frequencies are as follows:[1]* $\omega_t = \dfrac{\kappa_{e,eff}}{a_v C_{dl} l_t}$ *($\kappa_{e,eff}$: effective ionic conductivity of the electrolyte in the electrode, $a_v$: volumetric area of the EEI, $C_{dl}$: electric double-layer capacitance, $l_t$: electrode thickness),* $\omega_{ct} = \dfrac{1}{R_{ct} C_{dl}}$ *($R_{ct}$: charge-transfer resistance),* $\omega_d = \dfrac{D_{e,eff}}{l_t^2}$ *($D_{e,eff}$: effective diffusion coefficient).*

the data presentation influences the visual assessment of the spectra's correct shape. The *Journal of The Electrochemical Society* requires Nyquist plots to have a 1:1 aspect ratio of the real and imaginary axes to properly evaluate conformity to or deviation from the 45° slope or semicircular arcs.

The line segment in the high frequency range of a porous electrode introduces a new time constant $\omega_t$, which corresponds to the duration required for an AC perturbation signal to reach the bottom of a pore. In Fig. 2f, four characteristic frequencies ($\omega_t$, $\omega_{ct}$, $\omega_{ds}$, and $\omega_{de}$) are annotated, corresponding to the time constants of the ion conduction in the pore, the charge transfer at the EEI, the diffusion in solid particles and the diffusion in pore electrolytes, respectively.

Although EIS outperforms DC techniques in resolving multiple processes with distinct time constants, an excessive number of time constants within the limited bandwidth will inevitably lead to the overlapping of several time constants, making their resolution a challenging task.

Under the blocking condition, the real part of the impedance of a porous electrode at the low frequency limit is greater than that of its flat electrode counterpart by 1/3 of the pore resistance (to be further discussed in Fig. 3).

## Difference Between Model-Predicted and Measured Spectra

Closed-form analytic models are derived under simplified, one-dimensional (1D), and ideal conditions which typically assume uniformity in geometry, structure, or the interfacial and bulk properties. However, nonuniformities occur unavoidably along and across the electrode in practical systems. These include: (1) complex pore and particle structures (such as size distribution, shape variations, and fractal features); (2) time-dependent structural changes (e.g., dynamics of water saturation); and (3) spatial distributions of reactants, products, current density, and overpotential during high current density operation. These nonuniformities lead to frequency dispersion, which manifests as lines with slopes deviating from 90° at the low frequency limit, and from 45° at the high frequency limit (Fig. 2a and 2b). In the intermediate frequency range, the frequency dispersion manifests as depressed semicircles (Fig. 2c–2f).

In addition, the measurement results are affected by the limited capabilities of the equipment, including bandwidth and accuracy contours, as well as factors such as cable inductance and stray capacitance at high frequencies, non-stationarity of the test sample at low frequencies, ambient electrical noise, and the use of a two-electrode configuration instead of a three-electrode configuration.

## Modeling of EIS for Porous Electrodes

### Three Types of EIS Modeling

As an indirect technique, EIS requires a model for interpretation. Consequently, EIS studies involve a close interaction between models and measurement, as well as an intimate interplay between hardware and software development. The modeling of EIS for porous electrodes can be categorized into three types: analogical, analytic, and numerical. Analogical modeling employs an equivalent electric circuit (EEC) to simulate the response of electrodes to AC perturbations. For flat plate electrodes, the EECs with lumped elements, such as the Randles circuit,[3] can provide satisfactory predictions. In contrast, for porous electrodes, EECs with distributed elements in the form of a transmission line (TML), first developed by de Levie,[4] are frequently employed.[5] In practical applications, a constant phase element (CPE)[6] is usually used instead of a pure capacitor. While this versatile element can significantly improve

*(continued on next page)*

the fitting, the relationship between the circuit element and the pore structure or process parameters is not always clear. Analogical modeling, being simple, rapid, and intuitive, is the most widely used EIS modeling approach in the literature. However, it can also be the most misused or even abused approach, to the degree that some EIS experts regard EECs merely as analogs rather than true models. Indeed, using lumped EECs for porous electrodes, or employing CPEs just for a better fitting without any discussion about the underlying physics is considered poor practice.

Analytic modeling derives the governing equations in the frequency domain from those in the time domain using a small perturbation assumption and a Fourier transformation. Closed-form solutions as algebraic expressions can be obtained under simplified conditions, typically involving either uniform distributions or limiting cases in which certain processes become negligible. Compared to analogical or numerical modeling, the analytic solutions provide a direct link between the impedance spectra and the electrode parameters, which can be exploited to parameterize for the electrode satisfying the simplified conditions. Analytic solutions also make it easy to conduct parametric studies and to identify the rate-limiting processes. Analytic modeling demands both physical insights to find limiting cases so as to make drastic simplifications, and mathematical prowess to beat a way through the maze of coupled differential equations to find a closed-form solution, hence representing the fundamental advance in EIS methodology. Some EIS theorists even argue that the true power of EIS can only be realized with analytic modeling.

However, the analytic models often lack a straightforward correspondence with the basic elements in EEC. Therefore, the use of a box is recommended in EECs to represent processes that cannot be reduced to pure resistor, capacitor, or inductor.[7] For example, a Randles circuit may include a box representing a Warburg element in series with the charge-transfer resistance, to account for diffusion processes that may dominate the impedance in some systems in the low frequency range. The Warburg element, an analytic solution in itself, can be represented with a distributed EEC having a semi-infinite series of R and C elements. Therefore, there is not always a clear-cut distinction between the analogical and the analytic modeling.

Numerical modeling applies a small-amplitude perturbation of current or potential to the coupled nonlinear system of differential equations in the time domain for the porous electrode, and then calculates the impedance from the Fourier transformation of the input and output signals.[8] By exploiting the computing power of modern computers and advanced algorithms, it circumvents the difficulty in deriving analytic solutions for nonuniform conditions, while maintaining the richness of information contained in the system of differential equations. Numerical modeling can readily handle distributions, gradient design, multiphysics, etc. However, the interpretation becomes more challenging, as the features in the calculated spectra tend to become blurred due to the multi-dimensional distribution and the overlapping of concurring processes.

### Physical EIS Models of Porous Electrodes

Physical EIS models of porous electrodes have been elegantly reviewed by Lasia[9] and Huang.[10] While Lasia organized the model evolution primarily according to the explicit pore description, Huang organized it primarily via implicit pore description. Here the explicit pore description means the exact geometry of the pore or pores is treated in detail, and the intrinsic transport parameters are used. In contrast, the implicit pore description employs the averaged structural parameters of porous media (e.g., porosity, tortuosity, and specific surface area), and uses effective transport parameters corrected for pore structures. Explicit pore description is intuitive and capable of capturing the essential features of the porous electrode even with a drastically simplified picture of the porous media. However, it has difficulties handling complex pore structures at the electrode scale. In contrast, implicit pore description employs the measurable quantities of the porous media. In many cases, the analytic models derived from explicit and implicit descriptions are mathematically equivalent and convertible.

The physics treated in these models includes the interfacial and transport processes under different limiting cases. For the porous electrode under blocking condition, an analytic model for cylindrical pore considering only ionic potential drop in the electrolyte has been developed by de Levie,[4] initiating the use of EIS for studying the porous electrodes. The effects of pore shape other than cylindrical have been investigated by Levie,[11] Keiser,[12] and Lasia.[13] The effects of pore size distribution have been examined by Song.[14] The effects of the top layer capacitance of porous electrode have been treated by Jurczakowski.[15] The effects of fractality in double or triple scales have been simulated by Itagaki.[16] In cases where the electronic resistance and ionic resistance of the electrode are comparable, a closed-form solution was derived by Bisquert.[17]

For porous electrodes under non-blocking conditions, there are a greater variety of limiting cases as more combinations of processes can be conceived. At OCV, the impedance of a porous electrode with negligible electronic resistance is given by the same model developed by de Levie, and that for non-negligible electronic resistance is given by the same Bisquert model, with the interfacial impedance modified from a pure electric double-layer capacitance (Cdl) to $C_{dl}$ in parallel with charge-transfer resistance $R_{ct}$. For electrodes under small current densities, an analytic solution of pore impedance can be obtained when there is uniform potential yet nonuniform reactant concentration in the pore.[18] In the case of uniform concentration yet nonuniform potential,[13] or the general case when both concentration and potential gradients are present, a numerical solution is needed.[18,19] Notably, spectra corresponding to the uniform electrolyte potential yet nonuniform reactant concentration do not exhibit a 45° line segment in the high-frequency range.

In Huang's review,[10] four foundational theoretical works predating the de Levie model are first described to set the historical context. The classical de Levie model is then rederived, followed with a thorough analysis of its five simplifying assumptions. The major body of the review then recounts the modeling efforts to relax these assumptions. Specifically, Huang categorizes the extensions of the de Levie model into three directions: physics, structures, and orders. In the extension in physics, a general theoretical framework describing the AC response of porous electrodes is first developed using volume-averaging and coordinate transformation. Huang's formulation differs from Newman's approach[20] in that it provides explicit expressions for the ion activity coefficient and effective transport properties, accounting for both the ion size effect and the structural properties of the porous media. Then, a general analytic solution under uniform conditions is derived, from which four limiting cases are further identified. Notably, Huang's review adopts a didactic approach. Detailed derivation, as well as source codes, are included in the main text (49 pages) and supporting materials (36 pages), to facilitate the entry into analytic modeling for prospective EIS enthusiasts.

## Application of EIS to Porous Electrodes

### Choose the Right Sample and the Right Model for the Right Purpose

All three types of EIS modeling have their strengths and limitations. No single model can serve all purposes equally well. On the whole, analytic models seem to strike a good balance of simplicity, rigor, and versatility.

Nevertheless, the authors believe that the so-called physics-based, mechanistic model is not synonymous with, nor restricted to, analytic models. All three types of EIS modeling can be physics-based and mechanistic, depending on the test samples and operating conditions. The key to EIS application lies not merely in the models, but also in the matching of models with the test samples at hand and the issues in question. Identifying the right match is an iterative process that requires a systematic approach to both the design and the execution of the EIS acquisition, as well as to the subsequent data processing and validation. In short, one should choose the right sample and right model for the right purpose.

## Example Application of EIS in the Life Cycle of LIBs/PEFCs

EIS has been extensively applied throughout the life cycle of electrochemical energy devices, particularly during the stages of design and operation, as well as in the second-life applications of LIBs. Qualitatively, EIS is employed for mechanism exploration (LIB aging[21] and PEFC sub-zero-start failure[22]), rate-limiting intercalation step identification,[23] performance loss attribution in PEFC,[24] state monitoring to enable control in PEFC,[25] and early warning for thermal-runaway in LIB.[26]

Quantitatively, EIS facilitates the parameterization of the structural parameters (e.g., tortuosity of separator and electrode in LIB,[27] tortuosity of ionomer in PEFC,[24] pore size distribution,[14,28] contact area and triple phase boundary in SOFC[29]), interfacial parameters (e.g., double-layer capacitance[30]), kinetic parameters (e.g., charge-transfer resistance[31] and activation energy of ORR in PEFC[32]), and transport properties (e.g., Li ion transference number,[33] diffusion coefficients of adsorbed gasses on porous solid,[34] $O_2$ diffusion in the GDL[35] and CL,[36] and proton conductivity[37]), of the porous electrodes.

Recently, the scope of EIS application has been extended to the examination of the slurry behavior during the electrode fabrication stage (e.g., the visualization of particle dispersion during slurry mixing,[38] and the analysis of mass transfer during the drying of coated CL[39]). The extensive application of EIS in LIB and PEFC can be found in comprehensive reviews.[40,41] In what follows, the procedures and precautions for the most utilized EIS techniques are elaborated.

## Procedures and Precautions for the Most Utilized EIS Techniques

*Measurement setup* ▶ A common mistake for novices in impedance measurement is connecting a potentiostat with EIS capability to an operating cell under load. In this configuration, the measured EIS will include that of the load in parallel with the cell. The correct procedure is to put the cell under the total control of the potentiostat. That is, the potentiostat acts both as a DC load or charger, and as an AC perturbator and analyzer. For electrochemical devices such as LIBs and PEFCs, complications may arise as the operating current may exceed the limit of the potentiostat, which is typically below

1~2 A. In such cases, a current booster is required. However, for EIS measurement, the frequency response capability of the booster itself must be checked to ensure it covers the frequency range relevant to the processes of interest in the test sample.

*High-frequency resistance ($R_s$)* ▶ In PEFCs, the high-frequency resistance ($R_s$) primarily consists of the membrane resistance ($R_{mem}$), the contact resistance between the flow fields and the GDL ($R_{FF/GDL}$), the contact resistance between the GDL and the CL ($R_{GDL/CL}$), and the bulk resistance of the GDLs ($R_{GDL}$). This $R_s$ is typically measured at high frequencies ($\geq 1$ kHz). The specific frequency suitable for $R_s$ measurement varies with material properties, cell assembly, and testing conditions, necessitating the measurement of high-frequency impedance spectra to determine the intercept $R_{s,meas}$ with the real axis in Nyquist plots. The $R_{s,meas}$ is often affected by the high-frequency inductance (HFI) effects, particularly in low-impedance systems where HFI is large and can incur significant errors. To minimize the interference of HFI, the following measures are recommended: (1) minimizing the lead wire length, (2) reducing the loop area between current-carrying and voltage-sensing wires through tightly twisted-pair configurations, (3) maximizing the distance between current-carrying and voltage-sensing wires, and (4) reducing the cell assembly non-uniformity. However, since the HFI interference cannot be eliminated completely, it is recommended to maximize the upper measurement frequency to obtain more inductance information for subsequent fitting and correction.

Ideally, an inductor in series with $R_s$ appears as a line parallel to the imaginary axis in the fourth quadrant in Nyquist plots (Fig. 3a, $\alpha = 1$). However, frequency dispersion caused by the distributed inductance often results in a line or curve with an angle deviating from the imaginary axis (Fig. 3a, $\alpha_L = 0.75$), exhibiting behavior similar to a CPE with a non-integer exponent. In such cases, a CPE element $Z_{L,\alpha} = (j\omega)^{\alpha L} Q_L$, instead of a pure inductor, may be used for fitting and correction[42] ($Q_L$ is the pseudo inductance and $\alpha_L$ is the inductance dispersion coefficient).

For porous electrodes with poor electronic conductivity, such as the positive electrodes in LIBs, the non-PGM cathodes in PEFCs, or the anodes in PEM water electrolyzers, the $R_{s,meas}$ contains contributions from both the electronic and ionic resistances of the CL, $R_{s,CL}$, as shown in Fig. 3b.

One method to address this issue is to perform ex-situ measurements and sum up all the bulk and interfacial resistances ($R_s$) of the cell components other than the CL. The resistance of CL at high frequency ($R_{s,CL}$) is given by:

$$R_{s,CL} = R_{s,meas} - R_s = \frac{l_t}{\sigma_s + \sigma_e} \tag{3}$$

where $l_t$ is the CL thickness, while $\sigma_s$ and $\sigma_e$ denote its electronic and ionic conductivities, respectively.

The projection length of the high-frequency 45° line segment of CL on the real axis ($\Delta R_{s,CL}$) satisfies:

$$\Delta R_{s,CL} = \frac{l_t}{3\sigma_s} + \frac{l_t}{3\sigma_e} - \frac{l_t}{\sigma_s + \sigma_e} \tag{4}$$

Knowing the CL thickness allows both to be determined by solving equations (3) and (4) simultaneously.

Another method to address this issue, eliminating the need for ex-situ measurement, was developed by Kulikovsky.[43] This approach is based on the linear relationship of the imaginary part of the impedances ($Z_{CL,im}$) with $1/\sqrt{\omega}$ ($\omega = 2\pi f$, $f$ is the measurement frequency) at high frequencies, where the slope $k$ satisfies:

$$k = \left(1 - \frac{3\sigma_e}{2\sigma_s}\right) + \frac{1}{\sqrt{2\sigma_e C_{dl}}} \tag{5}$$

Knowing both the $l_t$ and the double-layer capacitance ($C_{dl}$) of the CL allows $\sigma_s$ and $\sigma_e$ to be determined by solving equations (4) and (5) simultaneously. Subsequently, $R_{s,CL}$ can be calculated according to equations (3), and $R_s$ is the difference $R_{s,meas} - R_{s,CL}$.
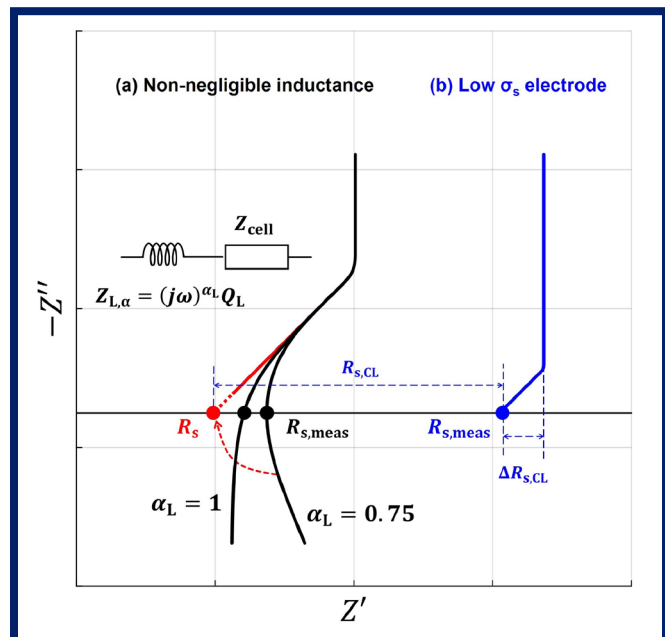


**FIG. 3.** *(a) The high-frequency Nyquist plot confounded by HFI (The black line) and the corrected plot (The red line); (b) The high-frequency Nyquist plot for electrode with poor electronic conductivity. The meanings of the symbols in the figure are as follows: $R_s$: high frequency resistance, $R_{s,meas}$: the resistance at the intersection of the measured high-frequency impedance spectra with the real axis, $R_{s,CL}$: the combined ionic and electronic resistance of CL at high frequency, $\Delta R_{s,CL}$: the projection length of the high-frequency 45° line segment of CL on the real axis.*

*Ionic resistance of the porous electrode ($R_{ion}$)* ▸ The estimation of the ionic resistance ($R_{ion}$) of cathode CL in a PEFC is based on de Levie's model under blocking conditions. Therefore, cyclic voltammetry (CV) should be performed prior to EIS measurements to identify the electric double-layer region and select a suitable measurement potential. As recommended by the New Energy and Industrial Technology Development Organization (NEDO),[44] the measurement potential is selected to be 0.45 V vs anode. After HFR
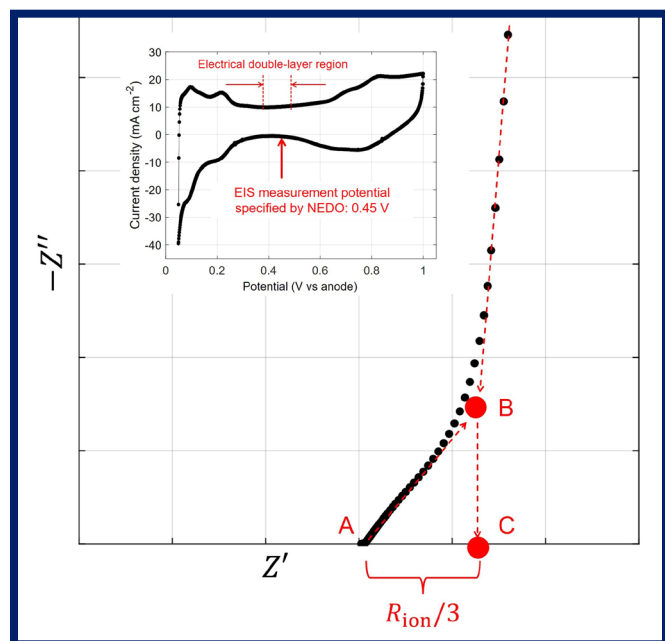
and HFI correction, the Nyquist plot typically shows a line segment at high frequencies with a phase angle of 45°. As the frequency decreases beyond the characteristic frequency $\omega_t$ of ionic conduction, the slope of the impedance spectrum increases sharply. However, due to the heterogeneous structure of the ionomer within the CL, this slope generally remains below 90°, making it inaccurate to estimate $R_{ion}$ simply by extrapolating the low-frequency line to the real axis. To address this issue, the NEDO protocol[44] (as shown in Fig. 4) recommends extrapolating the impedance lines on both the high and low frequency ranges to determine the intersection point B, and using the projection of B on the real axis to determine the $R_{ion}$. The length between points A and C equals 1/3 of $R_{ion}$.

In EIS measurements, it is important to minimize the impact of $H_2$ crossover from the anode. The rapid $H_2$ oxidation reaction at the cathode may distort the 45° line segment in the Nyquist plot, particularly in electrodes with low $R_{ion}$. The use of diluted $H_2$ is beneficial for diagnostics and parameterization.

*Double-layer capacitance ($C_{dl}$)* ▸ In electrochemistry, the double-layer capacitance ($C_{dl}$) is usually estimated using CV. Ideally, the charging and discharging current densities are proportional to the potential scan rates, with the slope being the $C_{dl}$. However, porous electrodes present complexities such as the distributed resistance and capacitance, and the adsorption and desorption, which collectively lead to CPE behavior. Additionally, the CV potential range may be restricted under certain testing conditions (e.g., CO adsorption on Pt surfaces). In such cases, estimating $C_{dl}$ via EIS may be beneficial.

Transforming the imaginary part of the impedance at low frequencies is a simple and commonly used method for estimating $C_{dl}$.[24] For a blocking electrode, its behavior approximates an ideal capacitor ($C_{dl} = -(\omega Z'')^{-1}$) at low frequencies in which the ionic penetration depth far exceeds the electrode thickness. Thus, $C_{dl}$ can be estimated from the imaginary parts of the low-frequency impedance, as indicated by the red line in Fig. 5a. For a non-blocking electrode with negligible mass transport resistance and current distribution, the equivalent electric circuit of the CL can be simplified to a parallel $R_{ct}\|C$ connection. The imaginary part of the impedance satisfies the equation $-(\omega Z'')^{-1} = (C_{dl}R_{ct})^{-1}\omega^{-2} + C_{dl}$. Plotting $-(\omega Z'')^{-1}$ against $\omega^{-2}$, the y-intercept of the line fitted to the low-frequency data points gives an estimate of $C_{dl}$,[30] as shown by the red line in Fig. 5b.

However, due to the complex structure of porous electrodes, this ideal behavior is rarely observed in measurement. More commonly, the measured data (black dots, Fig. 5a and 5b) deviate from the ideal case. Fitting the imaginary part of the impedance using an EEC
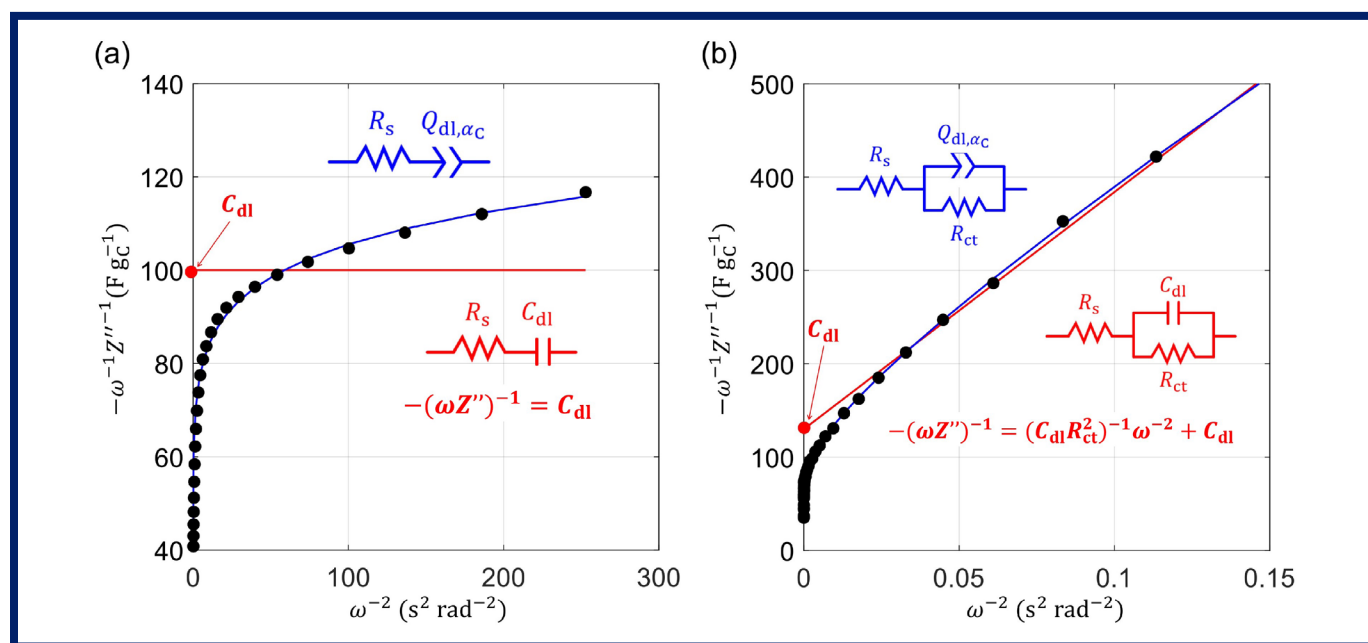


**Fig. 4.** *NEDO's protocol for estimating the CL ionic resistance ($R_{ion}$). In the electric double-layer region, similar impedance spectra are obtained under nearly blocking conditions. To standardize measurements, NEDO specifies 0.45 V vs anode as the potential for EIS measurement.[44] Point A is the intersection of the high frequency spectrum to the real axis after correction of HFI. Point B is the intersection of two asymptotic lines from the high and low frequency ranges of the spectra. Point C is the projection of point B onto the real axis.*



**Fig. 5.** *Comparison of double-layer capacitance estimation using EECs with pure capacitor vs CPE from the imaginary part of the impedance. (a) Blocking cathode CL under $H_2/N_2$ atmosphere at 0.45 V vs anode; (b) non-blocking cathode CL with $H_2$/Air atmosphere at 0.1 A/cm². The Pt loading of the cCL is 0.3 mg/cm². The catalyst used is TEC10V50E and ionomer-to-carbon ratio (I/C) is 0.6.*

with a pure capacitor results in significant errors (red line), whereas replacing the pure capacitor with a CPE yields a much better fit (blue line). For CPE behavior arising from the planar or normal distribution of resistance and capacitance, an equivalent capacitance $C_{dl,eff}$ can be calculated via well-defined formulas.[45] However, the CPE behavior in porous electrodes appears to be more complex, possibly resulting from the combined effect of two or more distributions. The challenge of how to accurately calculate the $C_{dl,eff}$ using the fitted pseudo-capacitance $Q_{C,a}$ and the CPE coefficient $\alpha_C$ remains unresolved.

In addition to the graphical methods mentioned above, it is also possible to estimate $R_{ion}$ and $C_{dl}$ using the transmission line model (TLM). This approach is applicable to both blocking and non-blocking electrodes. For non-blocking electrodes, the experimental conditions must be carefully controlled to minimize mass transport resistance, and the distribution of reactants, water, and current within the electrode, so as to closely approximate the model assumptions. Such conditions can be achieved by using a small-area cell, supplying pure $O_2$ at a high flow rate, and operating at a low current density. This approach is clearly demonstrated in the work of Baker et al.[46]

## Words of Caution and Consolation

Despite the power and elegance of EIS, the technique has several serious limitations that must be kept in mind. First, EIS is an indirect method, requiring models to interpret the measured spectra. Second, analytic models are only strictly applicable to idealized conditions like uniform distribution, one dimension, etc. In addition, modelers typically disregard practical issues such as noise and bandwidth limitations, which consistently plague experimentalists. Third, spectral resolution becomes challenging when two features with time constants within one order of magnitude coexist in the spectra.

To address the first limitation, researchers should complement and corroborate EIS results with other, non-frequency domain or non-electrochemical techniques. For example, the chemical diffusion coefficients of Li ions in cathode materials are measured using CV, EIS, and GITT, and are cross-validated.[47] The structural parameters estimated from the impedance data are critically compared with that extracted from 3D tomography.[48]

To address the second limitation, small or differential cells (with high stoichiometry ratios), or locally resolved EIS[49] can be used to mitigate in-plane non-uniformity. Alternatively, non-porous electrodes, such as single particles,[50] flat plate electrodes, or thin-film rotating disk electrodes (RDEs), can be utilized to avoid or minimize the influence of distribution in the porous electrodes. The measurable/reliable frequency range can be extended by choosing EIS equipment with a broader bandwidth, and by optimizing the electrode and the cell setup.[51] Noise can be significantly reduced by placing the entire test setup in a Faraday cage.

To address the third limitation, researchers can use graphical methods[1] or distribution of relaxation times (DRT) methods,[52] or systematically vary cell designs and operating conditions to enhance the feature recognition capability. On the other hand, symmetrical cells,[53] three-electrode setups with reference electrode tailored for impedance measurement,[54] or subjecting the cell to a blocking condition[55] can be employed to reduce the number of time constants.

Despite or because of these limitations, EIS, only a frequency-domain technique among the vast number of electrochemical methods, boasts its own dedicated international triennial symposium series (since 1989),[56] Asian biannual conferences (since 2015),[57] and European annual workshops (since 2008).[58] In the US, four-day annual short courses on EIS have been held since 1988.[59] Tutorials on EIS are common and well-attended at electrochemistry-related conferences.[60,61] Driven by the relentless efforts of theoretical modelers, data processing algorithm developers, and instrumentation providers, EIS has been continuously advanced with growing impact across electrochemistry, bioscience, environmental science, material science, sensors, and the semiconductor industry.

## Acknowledgement

## About the Authors

**YIMING ZHANG, PHD CANDIDATE, TSINGHUA UNIVERSITY SCHOOL OF VEHICLE AND MOBILITY**
**Education:** BS in Vehicle Engineering (Tsinghua University)
**Research Interests: Electrolysis and fuel cells** and Electrospinning
**Pubs + Patents:** 2 papers, 2 patents
https://orcid.org/0009-0004-9628-9474

**KEI ONO, RESEARCH ASSISTANT, TSINGHUA UNIVERSITY SCHOOL OF VEHICLE AND MOBILITY**
**Education:** BS in Chemistry (Koch University), MSc in Inorganic Chemistry (Koch University)
**Research Interests:** Electrolysis and fuel cells and Polymer rheology
**Pubs + Patents:** 7 papers, 9 patents
https://orcid.org/0000-0001-8018-2438

**JIANBO ZHANG, PROFESSOR, TSINGHUA UNIVERSITY SCHOOL OF VEHICLE AND MOBILITY**
**Education:** BS in Engineering Mechanics (Tsinghua University), PhD in Aerospace Engineering (The University of Tokyo)
**Research Interests:** Porous electrodes, EIS, Electrospinning, Fuel cells, Water electrolysis
**Pubs + Patents:** 101 papers, 20 patents
https://orcid.org/0000-0002-2964-8084

## References

1. J. Huang, Z. Li, B. Y. Liaw, and J. Zhang, *J Power Sources*, **309**, 82 (2016).
2. J. Huang et al., *J Electrochem Soc*, **162**, A585 (2015).
3. J. E. B. Randles, *Disc Faraday Soc*, **1**, 11 (1947).
4. D. Levie, *Advances in Electrochemistry and Electrochemical Engineering*, **6**, 329 (1967).
5. J. Moškon and M. Gaberšček, *J Power Sources Adv*, **7**, 100047 (2021).
6. G. J. Brug, A. L. van den Eeden, M. Sluyters-Rehbach, and J. H. Sluyters, *JEAC,* **176**, 275 (1984).
7. M. E. Orazem and B. Tribollet, *Electrochemical Impedance Spectroscopy*, Wiley (2008).
8. T. E. Springer, T. A. Zawodzinski, M. S. Wilson, and S. Gottesfeld, *J Electrochem Soc*, **143**, 587 (1996).
9. A. Lasia, in Modern Aspects of Electrochemistry No. 43, M. Schlesinger, Ed., vol. 43, 1–71, Springer New York, New York, NY (2008).
10. J. Huang et al., *J Electrochem Soc*, **167**, 166503 (2020).
11. R. De Levie, *Electrochim Acta*, **10**, 113 (1965).
12. H. Keiser, K. D. Beccu, and M. A. Gutjahr, *Electrochim Acta*, **21**, 539 (1976).
13. A. Lasia, *JEAC*, **397**, 27 (1995).
14. H.-K. Song, Y.-H. Jung, K.-H. Lee, and L. H. Dao, *Electrochim Acta*, **44**, 3513 (1999).
15. R. Jurczakowski, C. Hitz, and A. Lasia, *JEAC*, **572**, 355 (2004).

**Zhang et al.**
*(continued from previous page)*

16. M. Itagaki, Y. Hatada, I. Shitanda, and K. Watanabe, *Electrochim Acta*, **55**, 6255 (2010).
17. J. Bisquert, *Phys Chem Chem Phys*, **2**, 4185 (2000).
18. A. Lasia, *JEAC*, **428**, 155 (1997).
19. J. S. Newman and C. W. Tobias, *J Electrochem Soc*, **109**, 1183 (1962).
20. J. Newman and N. P. Balsara, *Electrochemical Systems*, John Wiley & Sons (2021).
21. N. Mellgren, S. Brown, M. Vynnycky, and G. Lindbergh, *J Electrochem Soc*, **155**, A304 (2008).
22. S. Wang, Y. Sun, F. Huang, and J. Zhang, *J Electrochem Soc*, **166**, F860 (2019).
23. S. Y. Vassiliev, V. V. Sentyurin, E. E. Levin, and V. A. Nikitina, *Electrochim Acta*, **302**, 316 (2019).
24. Y. Liu et al., *J Electrochem Soc,* **156**, B970 (2009).
25. P. Hong, L. Xu, H. Jiang, J. Li, and M. Ouyang, *Int J Hydrogen Energy*, **42**, 19156 (2017).
26. P. Dong et al., *J Electrochem Soc*, **168**, 090529 (2021).
27. B. Suthar, J. Landesfeind, A. Eldiven, and H. A. Gasteiger, *J Electrochem Soc*, **165**, A2008 (2018).
28. H.-K. Song, H.-Y. Hwang, K.-H. Lee, and L. H. Dao, *Electrochim Acta,* **45**, 2241 (2000).
29. A. Bertei et al., *Int J Hydrogen Energy*, **41**, 22381 (2016).
30. H. Iden and A. Ohma, *JEAC*, **693**, 34 (2013).
31. W. Maier et al., *J Electrochem Soc*, **159**, F398 (2012).
32. C. Song et al., *Electrochim Acta*, **52**, 2552 (2007).
33. F. Single, B. Horstmann, and A. Latz, *J Phys Chem C*, **123**, 27327 (2019).
34. T. Q. Nguyen and C. Breitkopf, *J Electrochem Soc*, **165**, E826 (2018).
35. A. El-Kharouf, N. V. Rees, and R. Steinberger-Wilckens, *Fuel Cells*, **14**, 735 (2014).
36. T. Reshetenko and A. Kulikovsky, *J Electrochem Soc*, **162**, F627 (2015).
37. Y. Liu et al., *ECST*, **11**, 473 (2007).
38. T. Kanamoto, D. Kawashima, P. A. Sejati, and M. Takei, *J Soc Powder Technol, Japan,* **61**, 413 (2024).
39. T. Suzuki, T. Nagai, and S. Tsushima, *J Therm Sci Technol*, **16**, JTST0012 (2021).
40. Z. Tang et al., *J Power Sources*, **468**, 228361 (2020).
41. P. Iurilli, C. Brivio, and V. Wood, *J Power Sources*, **505**, 229860 (2021).
42. I. Franzetti, A. Pushkarev, A.-L. Chan, and T. Smolinka, *Energy Tech*, **11**, 2300375 (2023).
43. A. Kulikovsky, *Electrochem Sci Adv,* **1**, e2000023 (2021).
44. M. C. Lefebvre, R. B. Martin, and P. G. Pickup, *Electrochem Solid-State Lett*, **2**, 259 (1999).
45. B. Hirschorn et al., *Electrochim Acta*, **55**, 6218 (2010).
46. R. Makharia, M. F. Mathias, and D. R. Baker, *J Electrochem Soc*, **152**, A970 (2005).
47. X. H. Rui, N. Ding, J. Liu, C. Li, and C. H. Chen, *Electrochim Acta*, **55**, 2384 (2010).
48. J. Landesfeind, J. Hattendorff, A. Ehrl, W. A. Wall, and H. A. Gasteiger, *J Electrochem Soc*, **163**, A1373 (2016).
49. I. A. Schneider, D. Kramer, A. Wokaun, and G. G. Scherer, *J Electrochem Soc*, **154**, B770 (2007).
50. K. Dokko et al., *J Electrochem Soc*, **148**, A422 (2001).
51. B. Łosiewicz, R. Jurczakowski, and A. Lasia, *Electrochim Acta*, **80**, 292 (2012).
52. B. A. Boukamp, *J Phys Energy*, **2**, 042001 (2020).
53. G. Portalis, E. Carrapa, B. Simon, and V. Vivier, *J Solid State Electrochem*, **25**, 1915 (2021).
54. Y. Hoshi et al., *J Power Sources*, **288**, 168 (2015).
55. J. Landesfeind, D. Pritzl, and H. A. Gasteiger, *J Electrochem Soc*, **164**, A1773 (2017).
56. X. Yong, J. Zhang, and V. Vivier, *Electrochim Acta*, **497**, 144420 (2024).
57. https://aeis.web.nitech.ac.jp/
58. https://www.tu-chemnitz.de/etit/messtech/iwis/index.php
59. https://eiscourse.com/
60. https://www.electrochem.org/advanced-impedance-spectroscopy
61. https://www.iahe-fcd.org/wfcc2025-workshop